A portable picometer reference actuator with 100 µm range, picometer resolution, subnanometer accuracy and submicroradian tip-tilt error for the characterization of

Metrologia

A portable picometer reference actuator with 100 μm range, picometer resolution, subnanometer accuracy and submicroradian tip-tilt error for the characterization of measuring instruments at the nanoscale

OPEN ACCESS
IOP Publishing | Bureau International des Poids et Mesures
Metrologia

Metrologia **55** (2018) 541–557
https://doi.org/10.1088/1681-7575/aaca6f

A portable picometer reference actuator with 100 μm range, picometer resolution, subnanometer accuracy and submicroradian tip-tilt error for the characterization of measuring instruments at the nanoscale

Marco Pisani[1] **and Andrea Giugni**[1,2]

[1] Istituto Nazionale di Ricerca Metrologica (INRIM), Strada delle Cacce 91, 10135 Torino, Italy

E-mail: m.pisani@inrim.it

Received 23 February 2018, revised 3 June 2018
Accepted for publication 5 June 2018
Published 29 June 2018

Abstract

We present the realization and the characterization of a picometer reference actuator (PRA), a metrological instrument based on a precision linear actuator capable of 100 μm range with subnanometer accuracy, picometer resolution, and submicroradian tip-tilt pointing control. The PRA relies on an integrated multiple reflections homodyne interferometer as a high resolution and accurate internal reference, on a multiple reflection based angle sensor for the control of the movement straightness, and on a versatile mirrors configuration to transfer the metrological traceability to an external device. As an example case we report the use of the PRA for the characterization of the non-linearities of the INRIM heterodyne interferometer dedicated to the calibration of capacitive sensors.

Keywords: metrological actuator, high-resolution interferometry, homodyne interferometer, optical path multiplier, optical non-linearity, metrological angle sensor devices

(Some figures may appear in colour only in the online journal)

Introduction

Dimensional measurements promote innovation and competitiveness in manufacturing through measurement science, services, and technical contributions to standards stimulating the realization of high-precision measurement techniques at the nanoscale. Dimensional measurements play a crucial role in almost every aspect of modern life, ranging over medical devices [1], optical sensors [2], microelectromechanical systems [3–5], integrated circuit technology [6], ICT, and cutting-edge nanotechnologies [7] where precise dimensions and standardization are paramount in product specification and quality certification. In particular, for dimensional metrology in semiconductor manufacturing processes [8, 9], laser interferometers are the unsurpassed standard for both pattern scaling on photomasks and for their alignment and precision overlap on multi-layered wafers densely populated by transistors whose transversal dimension can already reach the noticeable size of only 1 nm [10–12].

At present, many other nanofabrication sectors push to the routinely large-scale realization of a complex collection

[2] Present address: King Abdullah University of Science and Technology, (KAUST), PSE Divisions, Thuwal 23955-6900, Saudi Arabia.

of nanoscale devices. Their functional units are developed by continuously refining processes either bottom up, atom by atom, or top down like in single-atom layer chemical vapor deposition [13–16]. With the nanofabrication techniques it is possible to realize, for example, quantum plasmonic devices and metamaterial [17], nanoplasmonic resonator [18–20], and surface plasmon or single atom laser optoelectronic devices [21]. Also 2D ICT, based on graphene and on other functionalized layers of chalcogenides hybrid metals, has demonstrated new unique electronic behavior, with physical, chemical and mechanical properties that rely on the specific bonding structure on the nanoscale. Either the devices realization or the characterization instruments, such as most performing scanning probe and electron beam microscopes (e.g. AFM-STM Asylum Chyper [22], EBL Jeol JBX-9500FS [23], TEM FEI Metrios [24]) as well as metrological positioning stages [25] will benefit from an advanced metrological traceability. Recently, in biology and proteomic a single DNA strand with a base resolution [26] (single atom scale size), has been observed, with the intent of identifying nucleotides and their spatial conformation and to relate it to the specific functional expression in wildlife.

All the scientific and technological efforts require worldwide comparison and reproducibility, as well as the highest accuracy to give a reliable comparison with theoretical models, demanding the continuous development of novel compact metrological systems (namely optical interferometers) with non-linearities, noise, and stability at a nanometer level [10, 11].

The present work has been carried out within the European project NanoTrace [27, 28], a project aimed to achieve a 10 pm accuracy for displacement metrology. It focused on developing the next generation optical interferometers to meet the developments in standards and regulatory frameworks, the new technologies in scanning probe microscopy, and the advances in coordinate metrology.

The fundamental limit of optical interferometers is the periodical non-linearity, also referred to as cyclic error, it arises from the non-ideal behavior of optical components. The non-linearity and the methods to reduce the same have been subject to constant investigation [29–38], nevertheless, the accuracy of the better in the class of commercial instruments typically limits to hundreds of picometers. For the aforementioned critical uses the knowledge of such errors is mandatory. To characterize a high-performance optical interferometer an actuator having negligible (or known) overall errors must be used to displace the target mirror observed by the interferometer itself. Within the project NanoTrace, the ultimate performance of the interferometers [28] realized by researchers of the participating National Metrology Institutes (PTB, UME, INRIM, CMI and MIKES) have been defined by comparison with the x-ray interferometer (XRI) operating at the NPL laboratories [39, 40], which has an intrinsic picometer level accuracy. Unfortunately, the complexity of the XRI limits it usability opportunity, being practically unmovable from the laboratory. The need of a transportable actuator capable of picometer resolution and non-linearity for the characterization of high performance interferometers has been the driver of the present work. Furthermore, the candidate actuator must have extreme pointing capability (very low angle errors) to prevent alignment errors in the interferometer measurement. Precision actuators which have excellent resolution are commercially available [41], nevertheless neither the accuracy nor the tip-tilt errors are simultaneously good enough for the purpose. Therefore, a novel picometer reference actuator (PRA), has been designed, realized, characterized and tested.

In section 1 we describe the device detailing the functional blocks and control architecture. In section 2 we discuss the device tests and its performances. In the last section, we present and discuss a practical application case, namely the characterization of a heterodyne interferometer used for the calibration of mechanical probes.

1. The Overall structure of the PRA

The schematic functional principle of the PRA is shown in figure 1. The base is the mechanical reference of the device. A piezo actuator displaces the moving mirror M_M with respect to the fixed mirror M_F integrated into the base. The user measures the differential displacement d. The same displacement is observed by means of a reference laser interferometer integrated into the base, between the interferometer mirrors M_I. The difference between the user measurement and the reference interferometer measurement will give the errors of the first within the uncertainty and the resolution of the second.

Figure 2 is a sketch of the PRA with its main components that will be described in detail throughout the text. The main purpose of the actuator is to characterize laser interferometers namely in resolution and cyclic non-linearities. For this reason, the interface towards the user has been realized by a pair of fixed mirrors symmetrically displaced aside a moving mirror assembly so that a single beam or differential interferometers can be coupled indifferently.

The base structure, a $200 \times 200 \times 30$ mm block, and the user mirrors are made of *Clearceram*$^{@}$*-Z*, an ultra-low expansion glass-ceramic manufactured by Ohara Inc. (Japan). Characterized by a thermal expansion of $\pm 0.2 \cdot 10^{-7}$ °C^{-1} it assures long-term stability of all the sensible parts even in poorly thermalized environments. On the upper surface of the base, the internal reference interferometer is built, specifically a multi-reflections interferometer (described in par. 1.3), which measures the relative displacement between the fixed mirrors and the moving mirror, displaced by an actuator integrated in the base. The other optical elements are mounted on compact commercial precision mounts (FineAdjustment mod. Venus) fixed to the glass base using epoxy glue. The laser light feeding the reference interferometer is brought to the bench by means of an optical single mode polarization maintaining fibre (par. 1.4).

A particular effort has been made in developing and integrating into the base structure a simple and effective system to compensate the angular displacement error of the long-range translation stage (see par. 1.5).

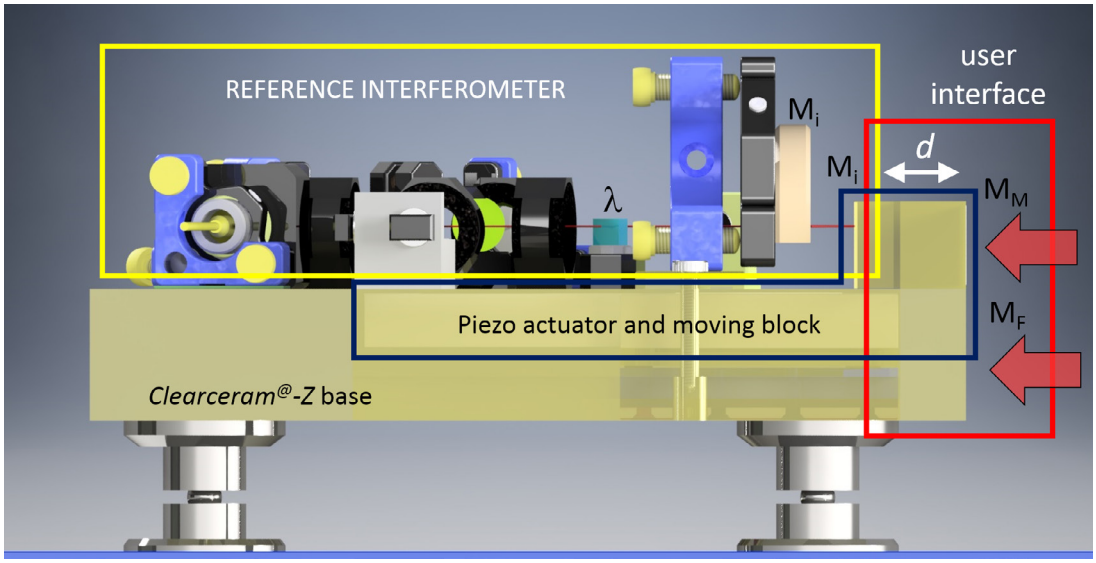

Figure 1. Schematic of the PRA working principle. The *Clearceram*$^{@}$*-Z* base is the mechanical reference of the device. A piezo actuator displaces the moving mirror M_M with respect to the fixed mirror M_F integrated in the base. The user measures the displacement d. The same displacement is observed by a reference laser interferometer integrated into the base, between the interferometer mirrors M_I.

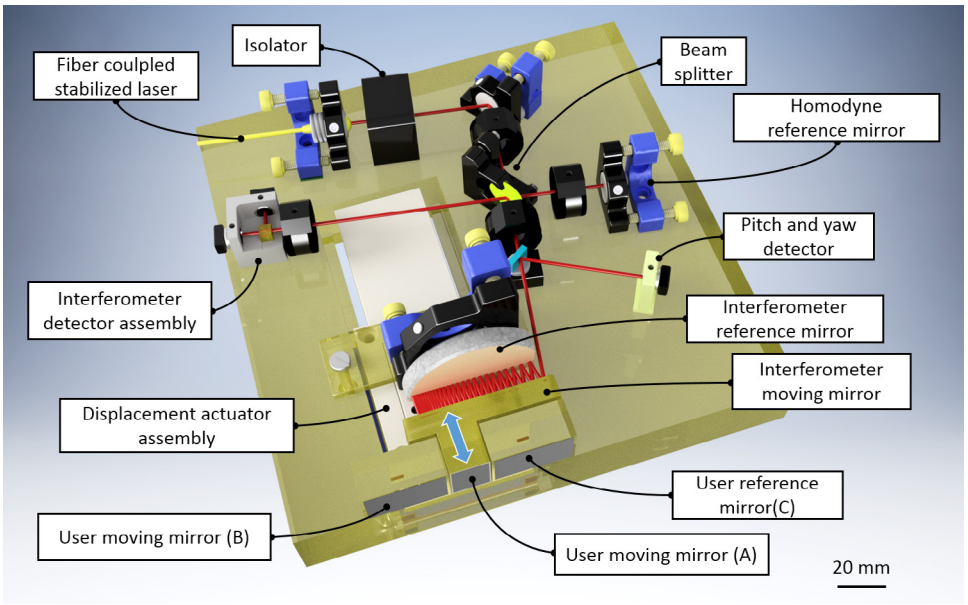

Figure 2. Mechanical design of the PRA. We have indicated the main mechanical elements and the optical ray propagation paths, from the optical fiber to the interferometer and tilt-control detector assemblies.

1.1. The mirrors assembly

The arrangement of the mirror structure is shown in figure 3. Two parallelepipeds bonded to the base having aluminium coated front face (highlighted with dashed red lines in the picture) identify the fixed user mirrors B and C. Also the front side of the base is coated with aluminium to be used as an auxiliary fixed mirror. These three mirrored surfaces are flat and nominally parallel (within 1 mrad). The central T-shaped block (highlighted with dashed yellow lines) is the only moving element displaced by the piezo actuators assembly described later (sections 1.2 and 1.5). Its front side, namely mirror A, is aluminium coated to offer the broadest optical reflectivity range for the user side. Mirror A is nominally parallel to the block backside, F, which conversely is multilayer dielectric coated for a maximal reflectivity value at the 633 nm wavelength ($R > 99.5\%$). The last block is tilt adjustable by means of a precision high stability 2″ tip-tilt mount (Fine Adjustment, Mars Series). It is coated with the same high reflectivity layer on its front surface, and it identifies the mirror E, which together with mirror F form the multireflection arm of the internal interferometer (described in par. 1.3). The possibility of tilting the 'fixed' mirror E allows trimming the angle between E and F. This allows one to change the number of multiple internal reflections N, to the desired value and to optimize the interferometer alignment. Both mirrors E and F have flatness $\lambda/20$.

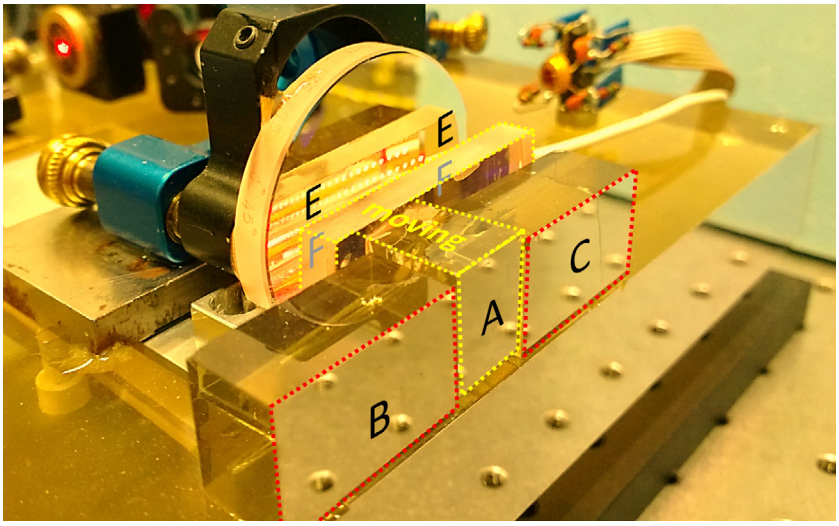

Figure 3. Detail of the mirrors assembly. Two aluminium coated blocks (highlighted in red in the picture) are the fixed user mirrors, B, and C. The central T-shaped block (highlighted in yellow) is the main moving element. Its front side, mirror A, is the moving user mirror. The block backside, mirror F, faces mirror E fixed to the base. The two are multilayer dielectric coated (for a maximal reflectivity value at 633 nm) and form the multi-reflection arm of the internal interferometer.

The three front mirrors A, B, and C are the 'user' mirrors for the calibration of the interferometers. Considering the simplest differential interferometer configuration, two beams are sent parallel towards the target (the PRA in this case) where one mirror is fixed (B or C) and one is moving (A), and the measurand is their relative displacement. In more advanced interferometers four beams are used (e.g. the ZMI-DPMI by Zygo): two as a reference and two for the measurement (see section 3). The adopted arrangement, a fixed and a moving mirror for the PRA, is versatile enough to host different interferometric configurations. We chose the three-mirror arrangement and their dimensions expressly to replicate the NPL XRI (mentioned above) already optimized for the same purpose. This choice allows for the same high-resolution interferometers usually compared with the XRI to be compared with the PRA.

Figure 4 shows a picture of the fully assembled PRA during an internal test phase.

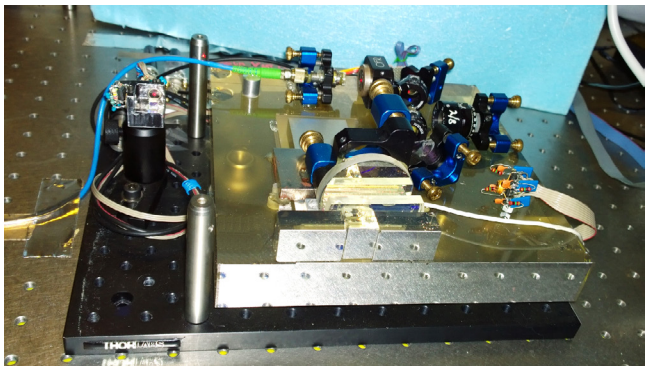

Figure 4. Picture of the assembled PRA: in the foreground, the user's mirrors are visible; in the background, the components of the reference interferometer are visibly glued to the ceramic glass base.

1.2. The main actuator, closed- and open-loop working approaches

The actuator used to move the block with A and F mirrors is based on a commercial piezo nanopositioning stage (Mad City Lab Inc. mod. Nano-OP100) that can be driven in closed loop by its own controller for a 100 μm displacement range with a stepped resolution of 0.2 nm (Nano-Drive™ controller, 20 bit DAC and 24 bit ADC directly accessible through a USB interface). The flexure hinges, which form the guidance mechanism, are cut into the aluminium structure using electric discharge machining providing a resonance frequency of 2 kHz with a 100 g load.

The resolution of the Nano-OP100 active control, although very high, does not allow us to achieve the goal of less than 10 pm level resolution. Also, the noise introduced by the active control (see par. 2.2) could be not compatible with high resolution applications. For these reasons, we have envisaged two ways of operating the PRA: closed and open loop.

In the closed loop mode, the position of the mirror is actively controlled by the Nano-OP100 driver in a deterministic way within the resolution of the driver itself. This mode is useful when deterministic, large range movements are required, e.g. ramps, sinusoidal or triangle wave modulations. The Nano-OP100 driver allows the *a priori* determination of the movement within a relative accuracy of the driver that itself is better than 10^{-4}, with nanometer uncertainty. In any case, the real displacement of the actuator is given by the PRA interferometer output with the resolution and accuracy discussed later.

In the open loop mode, the Nano-OP100 driver is switched off. A low noise high voltage driver [42] is connected to the piezo of the Nano-OP100 actuator allowing for a very low-noise movement, although, because of the intrinsic non-linearity of the piezo actuators, the displacement is not wholly deterministic. This mode is useful when very small movements must be applied to the mirror to the purpose of testing the resolution of displacement sensors in the subnanometer

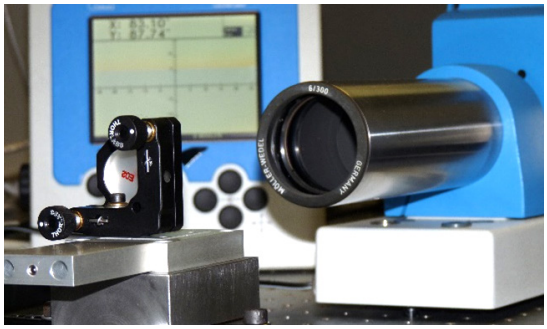

	left	centre	right
top	-8.6		15.8
	-23.5		-21.6
centre		1.9	
		18.1	
bottom	1.9		3.0
	27.5		15.5

Figure 5. Characterization of the straightness of the actuator used for the displacement of the mirror. Left: experimental set-up; right: synoptic table for the maximum yaw (yellow) and pitch (blue) errors relative to different positions of the load on the moving plate. The errors are in μrad p-p over the full 100 μm range.

range. Also in this case the real displacement of the actuator is given by the PRA interferometer output.

We proceeded to an accurate characterization of the performances of the Nano-OP100 considering the off-axis angular deviation error of the mirror movement one key parameter for the PRA displacement actuator. With the use of an autocollimator (Moeller Wedel mod. ELCOMAT 3000) we measured the tip-tilt rotations of a mirror secured to the moving part of the actuator while it elongates. The measurements were done for different loads and their different positions on the moving plate. The used setup is shown in figure 5 aside the results of a typical measurement. As a result, a relatively large rotation on both angles was observed along the scan. This prevented the direct use of the Nano-OP100 being its movement not accurate enough to satisfy the required performances of the PRA. In section 1.5 we describe the method developed to compensate the angular displacement error of the long-range translation stage.

1.3. The reference interferometer

The metrological reference of the PRA is the interferometer embedded in the structure which measures the displacement of the moving mirror. The principle and the mathematical details of the multiple-reflection interferometer have been extensively described in [43, 44]. In brief, in a multiple-reflection interferometer, the measurement arm is made of two quasi-parallel mirrors. The laser beam, entering with an incidence angle α, is reflected N times between the two mirrors acting as an amplification of the optical path. This scheme allows one to largely increase the resolution and to reduce the errors of the reference interferometer by a factor of N (typically about 80 for the PRA) with respect to a classical homodyne interferometer.

We show the optical layout of the PRA internal interferometer in figure 6 using a CAD rendering reconstruction. The laser beam exits from a fiber terminated with a collimation lens (H) passes through a Faraday isolator (I) and after a folding mirror (J) crosses a $\lambda/2$ waveplate (K) used to adjust the linear polarization orientation before entering in the interferometer. By means of a 50% glass plate beam splitter (L), the beam is divided into a reference beam, which is reflected by a fixed mirror (M), and a measurement beam, which goes to the multiplication section. This is constituted by the two high reflectivity mirrors F and G. After N reflections between F and G mirrors the beam is reflected back towards the beam splitter (L) for the recombination with the reference beam. The reference beam passes twice through a $\lambda/8$ waveplate (N) which transforms the beam polarization from linear to circular. Eventually, the two beams interference is revealed by the detector assembly (O) which generates the two quadrature signals as described in [44]. The $\lambda/2$ waveplate (P) placed in front of the detection assembly allows one to balance the amplitude of the two signals.

In principle, only the $\lambda/8$ waveplate is needed to obtain a sine and cosine signal for the phase measurement. In the practical realization, an auxiliary $\lambda/4$ waveplate (Q), have been inserted into the optical path to compensate unwanted polarization rotations occurring at the beam splitter and in the multi-reflection arm. By trimming the four wave retarders it is possible to balance the relative intensity and phase of the two signals to obtain almost ideal sine and cosine profiles. A further overall normalization is implemented numerically as explained later (par. 1.6.1). In the measurement arm is inserted a beam sampler (R), which addresses a small portion of the beam, coming from the multiplication mirrors towards the beam splitter, to a four quadrant detector (S) used to detect the tilt error of the moving mirror (see section 1.5).

1.4. The stabilized laser source

We have used a He–Ne stabilized laser made by SIOS GmbH model SL/02. The laser wavelength is stabilized to 10^{-8} level and calibrated at the INRIM facilities. One polarization, selected by means of a PBS cube, is fibre coupled and guided to the optical bench via a 2 m long single mode polarization maintaining fibre. The output collimator, fixed on the bench via a steering mount can be considered the built-in laser source of the reference interferometer allowing one to keep the heat source generated by the laser far from the sensitive interferometer parts. Particular care has been taken to avoid vibration-induced stresses of the fibre, recognizing that all rotations of the polarization couple with the faraday isolator, causing a non-negligible modulation of the laser power feeding the interferometer. Experience teaches that amplitude modulation can cause small phase noise that can be critical in very high resolution applications. In turn, during the stage scan,

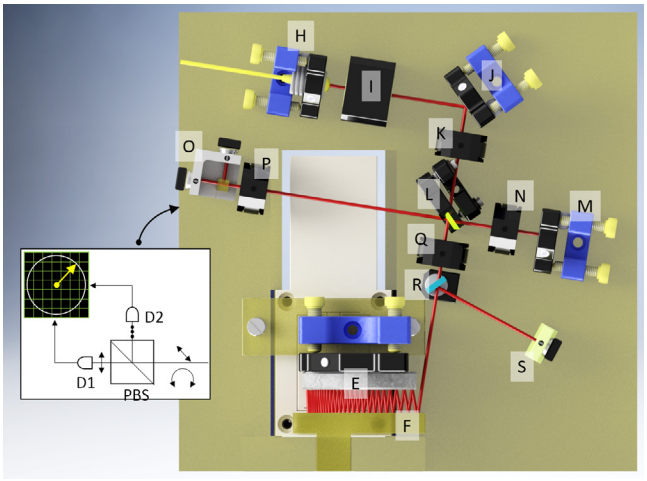

Figure 6. Optical layout of the interferometer used as the PRA internal reference: (H) fiber collimator on tip-tilt mount, (I) Faraday isolator, (J) steering mirror, (L) beam splitter, (M) reference mirror, F and G moving and fixed mirror of the multiplication assembly, (N) $\lambda/8$ retarder, (K and P) $\lambda/2$ retarder, (Q) $\lambda/4$ retarder, (R) beam sampler, (S) four quadrant detector. In the box on the left the detail of the detector assembly (O).

this amplitude modulation couples with non-linearities contributing with a phase noise to the signal, resulting in a critical issue in very high-resolution applications. The laser power at the output of the collimator was about 0.8 mW, adequate to obtain an excellent signal to noise ratio at the detector level.

1.5. The angle detection and the 'pentapode' actuator

The parallelism of the mirrors is a fundamental requirement for the accuracy of interferometric measurements. As said in paragraph 1.2 the piezo actuator residual tip-tilt errors are not acceptable for the purposes of the PRA. Furthermore, good parallelism is also needed to keep the alignment of the multi-reflection interferometer over the full displacement range. Therefore, a system to detect and correct tip-tilt errors has been built.

The detection system is based on the same laser beam used for the interferometer, picked up after the multiple reflections between the two mirrors E and F. When the interferometer is aligned and the F-mirror movement is parallel to itself, the reflected beam is superimposed to the outgoing beam. As soon as the mirror rotates, the beams undergo a rotation equal to the one of the mirror multiplied by the number of reflection on the same mirror [45] causing a large angular spread of the returning beam. Said rotation, combined with the laser path length causes a lateral displacement of the returning beam. A small portion of this beam is extracted by a beam sampler ($\approx$4%) and sent to a four quadrant detector which generates two electrical signals proportional to the vertical and horizontal rotation of the mirror (see figure 6). These two signals are used as error signals by the angle control unit.

For the correction of the angle errors, we have built the actuator shown in figure 7. Five piezo actuators control the movement of an upper stage supporting the Nano-OP100. They are connected to a lower base plate fixed to the main glass structure of the PRA. Two piezos work in parallel to lift the back of the stage implementing the pitch angle, other two work on the horizontal plane in a push-pull mode to implement the yaw angle. The last one works longitudinally to push back and forth the stage in parallel to the main actuator axis (x-axis) and can also be used to move the user mirror by small displacements to fill the gap between consecutive Nano-OP100 steps when used in closed loop. Load springs are used to counterbalance the piezo action. Because of the five actuators configuration, we have named the device as 'pentapode' although in fact it controls only three degrees of freedom. The five identical piezo actuators have about 5 μm range with 100 V leading to a tip tilt range of about 60 μrad (12 arcsec), enough to compensate the OP-100 errors. The pentapode has been characterized by using the cited autocollimator applying different voltage ramps to the pitch and yaw controls. The results are described in section 2.1.

We investigated the sensitivity and the independence of the two axes (horizontal and vertical rotations) to validate the actuator. We have used a set-up similar to the one shown in figure 5 where an autocollimator ELCOMAT 3000 aims at a mirror fixed to the pentode while the voltages applied to the piezos are changed. Figure 8 shows the result of the characterization done for the horizontal and vertical deflection angles respectively graphed versus their driving voltage in panels (a) and (b). Starting from the characterization of yaw angle (figure 8(a)): we measured both yaw (blue) and pitch (pink) curves applying a triangular ramp to the horizontal moving piezo actuators, 0–110 V. The measurement was repeated three times for three different constant voltages applied to the orthogonal axis (pitch): respectively 0, 55 and 110 V. It can be observed that the three blue curves have linear trend and overlap, meaning that the yaw control was independent on the value of the pitch angle. Furthermore the orthogonal pitch angle resulted constant while yaw was modulated. The results were confirmed by the curves of figure 8(b) obtained applying the complementary procedure to the same quantities. That means good orthogonality between the two actuators, allowing the correct operation of the two independent control loops. The two sensitivities (angle versus voltage) resulted 1.06 μrad V^{-1} for the yaw control and 1.17 μrad V^{-1} for the pitch control.

These results allow us to compensate for pitch and yaw errors within a range of about 100 μrad for the yaw and about 140 μrad for the pitch that is enough for our purpose.

1.6. The software, the electronics and control loops

The overall control of the interferometer requires the handling of two analog input signals proportional to sine and cosine of the interferometer phase ϕ, and the signals from the four quadrant photodiode used to monitor the autocollimation condition and to correct the tip-tilt angle. The interferometer sine and cosine signals are digitized employing a multifunction data acquisition module (NI USB-6251) that performs up to 1 Msample s^{-1} (aggregate mode) with 16-bit resolution. Signal acquisition is performed via

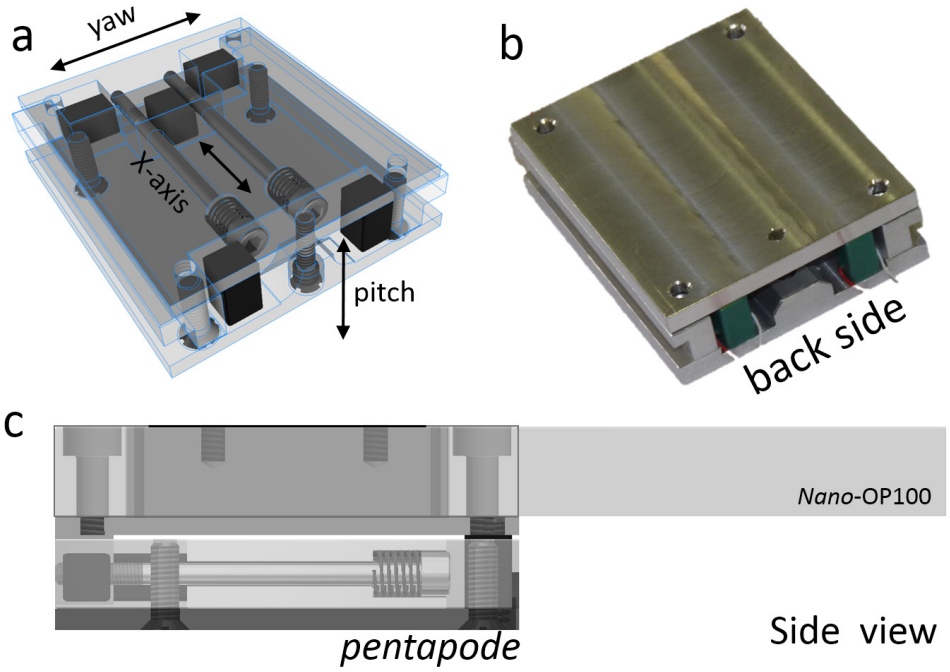

Figure 7. (a) CAD representation of the pentapode; the five piezos are in black, the light grey structure is fixed to the PRA base, the top grey part is the moving one. (b) Picture of the assembled pentapode with the actuators for the vertical angle visible at the back-side. (c) CAD representation of the Nano-OP100 transducer fixed to the moving part of the pentapode.

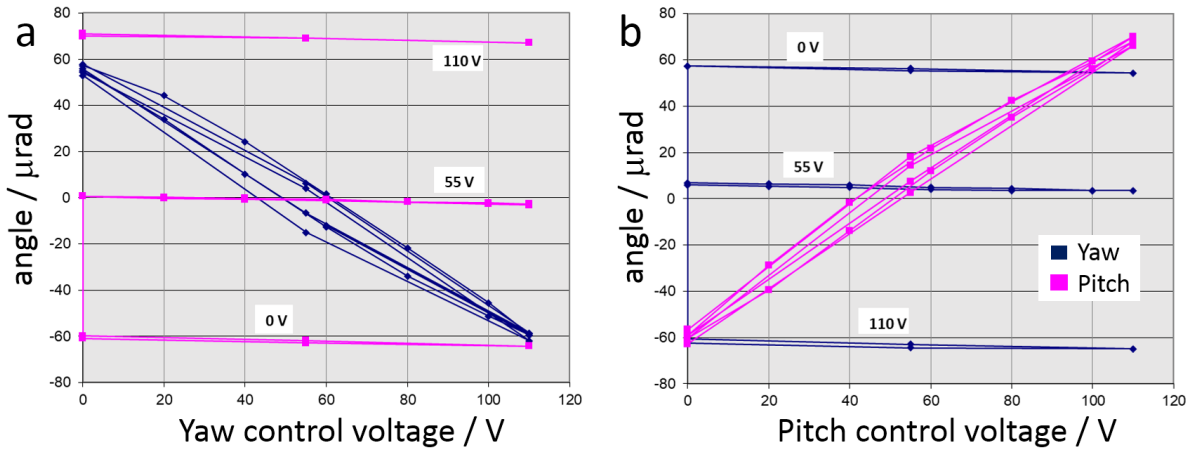

Figure 8. Characterization of the pentapode actuator. (a) Characterization of the horizontal (yaw) angle control. The voltage applied to the yaw actuator is driven in steps from 0 to 110 V (blue curve), while the voltage applied to the pitch actuator is kept constant. The measures shown are for three different values of the pitch voltage 0, 55 and 110 V. (b) Characterization of the vertical (pitch) angle control applying the same procedure.

an *ad hoc* software written in LabView®. An analogic circuit conditions the angle control signals.

1.6.1. Software for normalization and fringe counting. To have the desired linear phase-displacement function, normalization of the two signals coming from the photodiodes is mandatory. A correction in amplitude and offset is needed to consider the two signals as real sine and cosine. We chose not to act electronically on the quadrature of the two signals in order to reduce the possibility of systematic errors coming from the electronics. Quadrature correction, as explained in paragraph 1.3, is made by trimming the retarder plates in the interferometer. Assuming that the two signals are in quadrature, the signals x and y detected by the photodetectors D1 and D2 can be written as

$$\begin{aligned} x &= A\cos\varphi + p \quad \notin [-1,1] \\ y &= B\sin\varphi + q \quad \notin [-1,1] \end{aligned} \tag{1}$$

where φ is the phase to be measured, **A** and **B** are the scale factors, **p** and **q** are the offsets. To find these values, we need to collect enough data of the original sinusoids in order to have at least one maximum and one minimum value corresponding to the positive and negative peaks of the curve, practically a complete phase rotation, at least. For each x and y set of data the *scale factor* is evaluated as the half range and the *offset* as

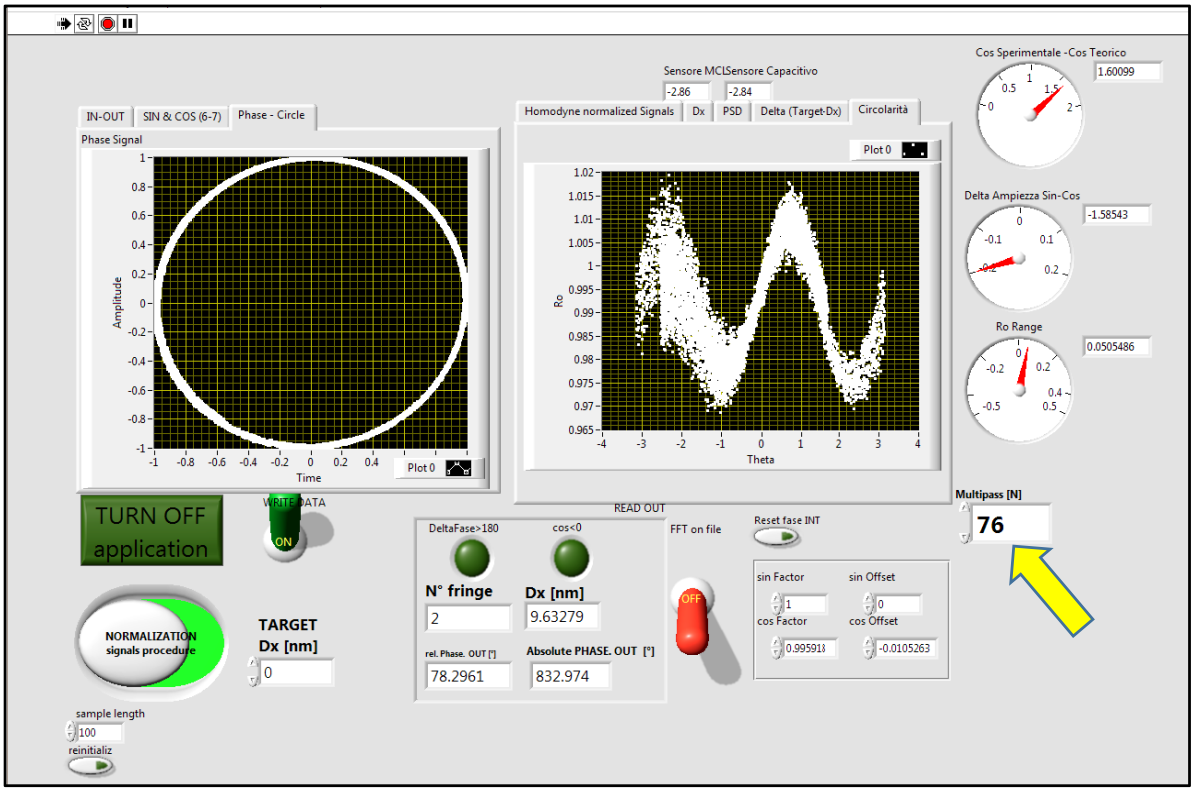

Figure 9. Control panel of the PRA software. The left and the right screens have multiple functions that can be chosen by the user. In the represented case, the PRA is moving its mirror at a constant speed; the left screen displays the phase circle plot; the right screen displays the distortion of the phase circle with respect to a perfect circle. The yellow arrow indicates the box where the number of reflections is digitated manually.

the middle value between maximum and minimum and they are stored as fixed values to modify the incoming data.

The modified new signals will be then

$$\begin{aligned} \cos\varphi &= (x-p)/A \quad \in [-1,1] \\ \sin\varphi &= (y-q)/B \quad \in [-1,1]. \end{aligned} \tag{2}$$

Here, we conveniently distinguish two possible working modes: a quasi-static and a dynamic mode. The quasi-static mode implies that the phase for any data buffer acquired by the DAC board spans only a small portion of the phase circle. In this case, to normalize the fringe, we need a preliminary scan of the device to store within the data buffer one or more phase revolution that corresponds to a minimum of about 4 nm. The normalization values are then calculated, stored and successively applied during the measurement phase. In the dynamic mode, i.e. when the PRA is moved long and fast enough (e.g. during a linear scan), each data buffer contain several phase revolutions allowing the normalization parameters to be calculated and updated in real time for each buffer.

Once normalized, the two signals are sent to a LabView routine which calculates and unwraps the phase vector. Then the phase is multiplied by the wavelength of the laser in air and divided by the constant N of the multi-reflection interferometer. The reading of the reference interferometer is the numerical output of the PRA. This number is saved, and the power spectral density is constantly calculated.

The graphic interface provides, aside from other informative boxes and controls tabs, the real-time phase circle representation and the averaged power spectral density analysis of the time signals. Both capabilities are used to check the correct alignment of the interferometer routinely. Furthermore, a qualitative indication of the distortion circle is displayed on request. In figure 9 is shown the PRA user interface. Two displays are always on: the user can choose the function of each one during operation. In figure 10 are shown the possible functions graphed on the two displays.

1.6.2. Angle control loop. The straightness of the F-mirror movement is checked by extracting a 4% of the beam exiting from the multiplication path and addressing it on a four-quadrant detector. Four trans-impedance amplifiers and a sum-difference circuit extract two signals representing the vertical and horizontal unbalance of the light spot on the quadrant detector. An auxiliary sum signal can be used to monitor the power of the laser. The quadrant detector is pre-aligned so that when the auto-collimation condition of the multi reflections interferometer is satisfied, the two signals are zero. The vertical and horizontal unbalances represent respectively pitch and yaw errors of the mirror movement and thus are used as error signals for two independent closed control loops (proportional-integrative) acting on the pentapode to keep the movement straight. The piezo actuators of the pentapode are driven by four low-noise HV amplifiers: one for the vertical piezos, two for the push-pull horizontal piezos and the last for the auxiliary longitudinal piezo.

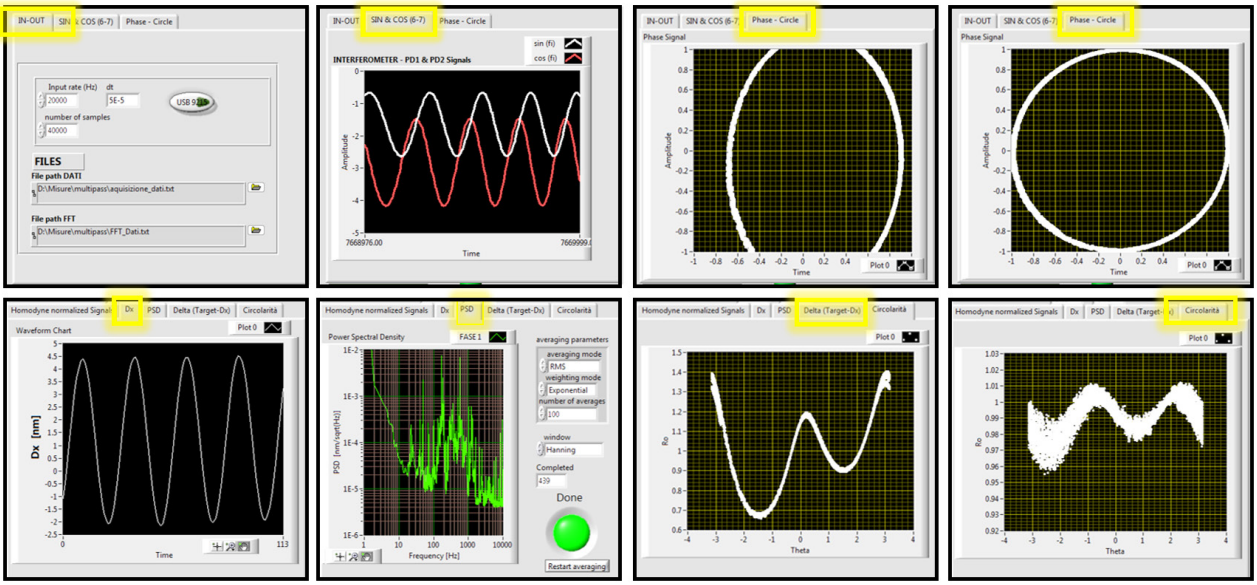

Figure 10. Screenshots of the control monitors available in the graphic interface. Upper row refers to the left screen in the control panel. From left: setting of the acquisition parameters (the sampling frequency and the number of acquired samples); displaying the raw acquired signals from the photodiodes; displaying the phase circle (before and after the normalization). Lower row refers to the right screen in the control panel. From left: time plot of the calculated displacement in nanometers; plot of the noise spectral density in nm $\sqrt{\text{Hz}^{-1}}$; distortion of the phase circle (before and after the normalization).

1.6.3. Control strategy. In figure 11 we show the block diagram of the PRA controller. The optical path, the electrical and the mechanical links are indicated with arrows. The diagram summarizes the role of the PRA building blocks described so far. The blue box highlights the Mad City Lab Nano-OP100 piezo linear stage with its integrated displacement sensor and the control loop. The sensor and the control are used in the closed loop operation mode (see par. 1.2). In the open loop mode the input is directly sent to the piezo through an HV amplifier and the Nano-OP100 control is ignored. The orange box highlights the angle control. This control loop is always on. The Nano-OP100 piezo actuator, connected to the PRA base through the pentapode tilter, moves the mirror block which in turn is measured by the interferometer. Finally, the user measures the displacement of the same mirror block and compares his results with the numerical output coming from the interferometer software.

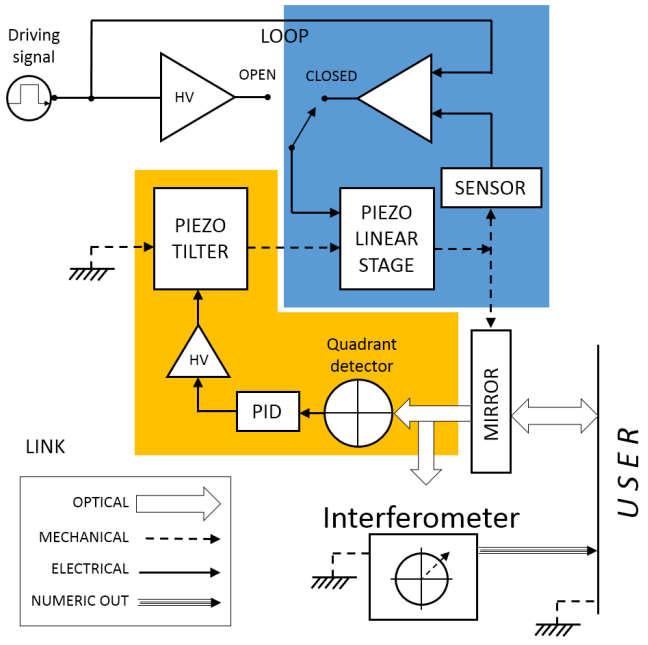

Figure 11. Block diagram of the PRA control. Arrows indicate the optical path, the electrical and the mechanical links. The blue box highlights the Nano-OP100 piezo linear stage with its integrated displacement sensor and the control loop. The orange box highlights the angle control. See text for details.

2. Experimental results and characterization

In this section, the characterization of the performances of the PRA regarding the straightness of the mirror movement and of the reference interferometer resolution and noise are presented.

2.1. Angle control performance test

To verify the effectiveness of the active angle control functional part, used to keep straight the displacement of the moving mirror as described in paragraph 1.5 and in 1.6.2, the following test has been performed. The PRA mirror is moved back and forth under the interferometer control over the full 100 μm range of the Nano-OP100 actuator. The active angle control keeps the error of the angle sensor close to zero by acting on the pentapode. An autocollimator aiming at the moving mirror (mirror A of figure 3) measures tip-tilt deviations while the displacement of the mirror is recorded. The measurement has been repeated several times with similar results. Typical results are displayed in figure 12. The residual pitch and yaw errors are respectively within 0.9 and 0.5 μrad p–p for the full range of the PRA.

2.2. Reference interferometer resolution and noise

The output noise of the actuator, including its thermal, mechanical and electronic noise, limits the resolution of the PRA. Thus the ultimate resolution is a frequency dependent parameter which we quantified by measuring the noise spectral density, NSD, of the interferometer output while driving the actuator with a null signal. We show in figure 13 the NSD recorded in different conditions: the red curve represents the PRA noise when working in open loop with the angle control function is active (i.e. the Nano-OP100 control switched off); the green curve is the noise of the electronics including the detector, the ADC board, and the quantization noises. This is obtained by switching off the laser, and it represents the detection limit of the optoelectronics. The blue curve is obtained with the laser switched on and the measurement arm of the interferometer blocked. This spectrum is an indication of the contribution of the laser amplitude noise to the interferometer output. Finally we report the grey curve as the noise of the PRA when working in closed loop, i.e. with Nano-OP100 control switched on. The measurements were performed on a passively damped optical table in an underground laboratory at INRIM which is thermally stabilized to (20.0 ± 0.1) °C. A wooden box, enclosing a portion of the table, was used to create a turbulence-free environment. Observing in detail the open loop noise of the PRA starting from very low frequencies we see that the noise is of the order of a few nanometers at 1 mHz than goes rapidly below 1 nm $\sqrt{\text{Hz}^{-1}}$ and reaches the 1 pm $\sqrt{\text{Hz}^{-1}}$ at few hertz. This typical low frequency behavior can be likely explained with thermomechanical drift of the overall structure, in particular of the less rigid parts i.e. the moving stage of the PRA (composed by the pentapode plus the Nano-OP100). The noise visible between few tens of hertz to few kilohertz are mainly due to the residual acoustic and vibrational energy coupling with the mechanical resonances of the moving stage of the PRA. These contributions reduce with frequency until the electronic noise dominates them at a level of few fm $\sqrt{\text{Hz}^{-1}}$. The residual narrow peaks in the kilohertz range are likely due to electrical interference noise, indeed are visible in all spectra. One could observe, by comparing the red and the blue curves that part of the noise seems to be attributable to the laser power noise, mainly in the low-frequency range.

We can conclude that the PRA noise when operating in open loop mode is less than 1 nm $\sqrt{\text{Hz}^{-1}}$ for frequencies higher than few mHz and goes down to 1 pm $\sqrt{\text{Hz}^{-1}}$ and less for frequencies higher than a few Hertz. When operating in closed loop mode, under the control of the Nano-OP100 driver, the noise is dominated by the control electronics of the same. Although quite higher than the open loop mode, the noise of the PRA in closed-loop, considering the 100 μm full range of the actuator, is remarkably good.

Another way to show the extremely high resolution of the PRA is to observe the time plot of the reference interferometer when the mirror is moved with a very low driving signal. In figure 14 is shown the PRA output when the piezo of the Nano-OP100 is driven in open loop with a 10 μV p–p square wave corresponding to a 10 pm p–p displacement. The driving

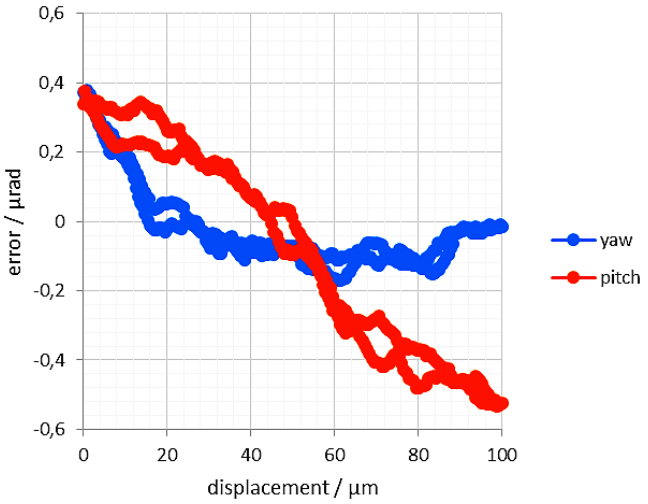

Figure 12. Measures of the residual error of pitch and yaw angles when the angle control loop is active. The Nano-OP100 is driven with a triangular ramp to the full 100 μm range. The graph is obtained by averaging 5 complete back and forth scans for a total measuring time of 1400 s.

signal is generated by passive attenuation (80 dB) of a 100 mV p-p signal in order to avoid errors at the microvolt level. The high signal to noise ratio is evident also at the picometer scale. Note that 10 pm is 10^{-7} of the full range of the PRA.

2.3. Reference interferometer accuracy/linearity

The accuracy of an interferometric measurement depends mainly on the alignment of measurement axes (cosine errors), the straightness related errors (Abbe errors), the knowledge of the laser wavelength λ including the effect of the air refractive index n and the non-linearity of the phase/displacement function. Furthermore, in the case of the multi-reflections interferometer, the accuracy depends also on the number of reflections N and a correction factor γ related to the multi-reflection geometry.

Regarding the alignment, assuming a conservative maximal parallelism error between mirror A and mirror F of 1 mrad, the cosine error associated to the measurement of mirror A displacement along its normal is about $5 \cdot 10^{-7}$, leading to a maximum of 50 pm over the full 100 μm range.

Regarding the Abbe error, we have to consider the combined effect of the straightness error of the moving mirror with the offset between the internal reference interferometer and the user interferometer axes. In fact, the internal multi-reflection interferometer has a distributed measurement area, but we can assume that the 'virtual' measurement axis coincides with the average position of the multiple reflection positions. This has been estimated to be within ± 1 mm to the center of mirror A. Assuming a worst case 1 μrad p–p straightness error, combined with a worst case 1 mm distance between the measurement axes, the maximum Abbe error will be 2 nm p–p over the full range.

Regarding the knowledge of λ, thanks to the laser stabilization circuitry together with the calibration against the national length standard, we can state that the maximum relative error

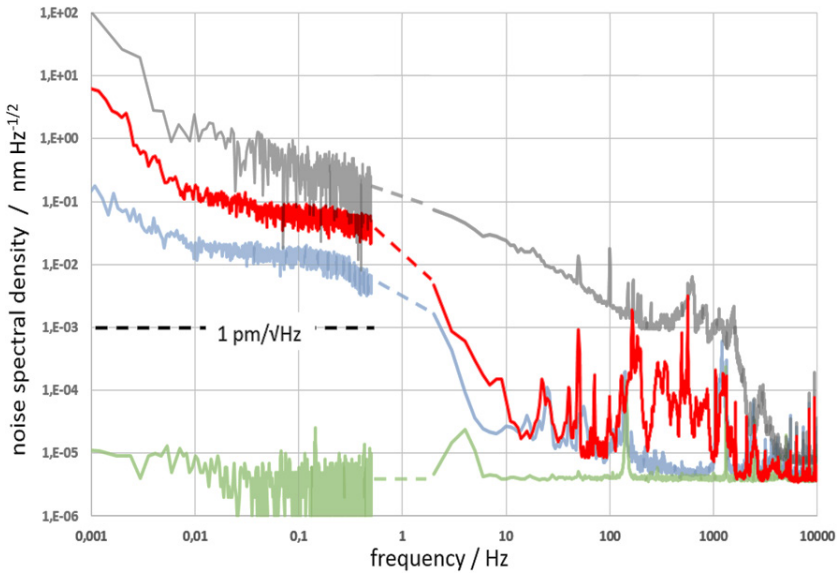

Figure 13. Noise spectral density of the interferometer. The red curve is the noise of the interferometer when the control of the piezo actuator is off (open loop mode), the grey curve includes the noise of the piezo actuator electronics (closed loop mode). See text for detail.

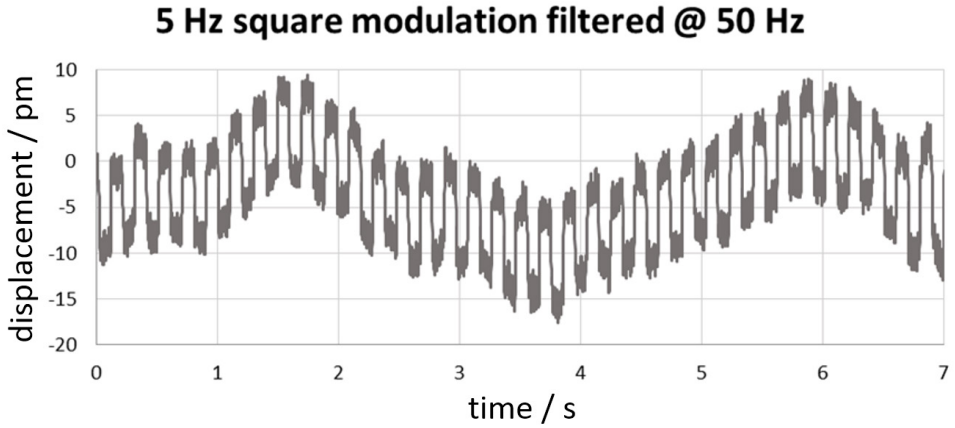

Figure 14. Time domain resolution test. The piezo of the Nano-OP100 is driven in open loop with a 10 μV p–p square wave corresponding to 10 pm p–p $= 10^{-7}$ of the full range of the PRA.

associated to λ is $5 \cdot 10^{-8}$, which is negligible compared to the effect of the air refractive index n. The latter is estimated using the Edlen [46, 47] formula with the environmental parameters of the laboratory. The maximum relative error associated to λ is $5 \cdot 10^{-7}$.

Regarding the phase/displacement function, being this the more critical uncertainty term, a detailed discussion is given in par. 2.3.2.

Regarding the knowledge of the multiplication factor N, in fact we cannot properly call it an uncertainty source since it is an exact number, nevertheless it must be known without ambiguity, if not the error would be larger than the percent. A discussion about how to find the exact value of N is in paragraph 2.3.1.

In a multi-reflections interferometer, because of the non-zero incidence angle (α), each reflection on the moving mirror is not orthogonal to the displacement; furthermore, the mirror displacement causes a lateral shift of the whole reflection pattern. The combination of these two effects causes a deviation f from the gain calculated as if α was zero of the order of few parts per thousand. The correction factor is function of N and α according to the exact formulae reported in [44]. Given a value for N, an error must be associated with the estimation of α. In our case, we have measured α with an uncertainty of 100 μrad leading to a proportional error of the correction factor of $6.6 \cdot 10^{-6}$.

Finally, an uncertainty budget is given in par. 2.3.3.

2.3.1. Evaluating the number of reflections. The integer number of reflections N is to be known without ambiguity, however its determination it is not straightforward. It is challenging to count the number of reflections by looking at the spots pattern on the mirrors or estimating it by measuring the angles in the multiple reflection set-up. For these reasons we adopted two alternative methods. The first is to compare the output of the PRA software, considering N as a parameter to be determined, with the output of the interferometer to be characterized by the PRA for a relatively large displacement (of the order of micrometers). If the proposed number is incorrect the difference between the two readings will be huge (more

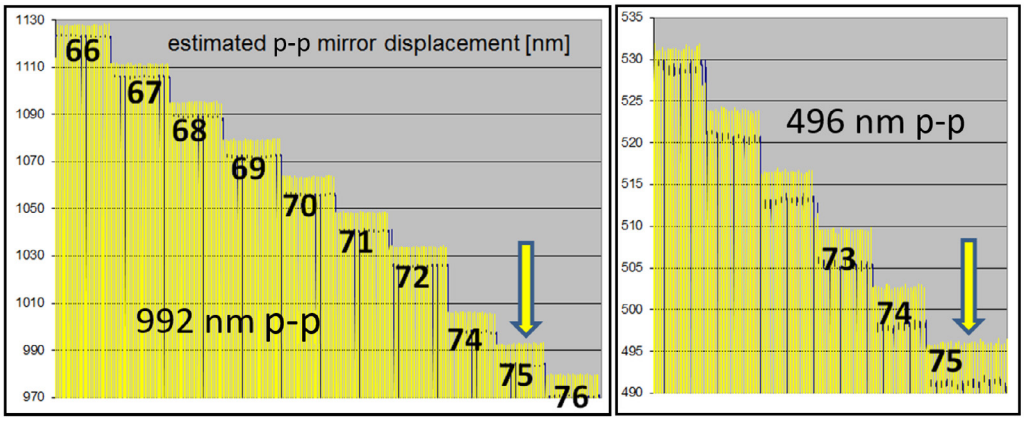

Figure 15. Determination of the multiplication factor N. The comparison of the output calculated by the interferometer software (yellow graphs) with the nominal displacement of the piezo actuator (992 and 496 nm respectively) allows one unambiguously find the integer number corresponding to the number of reflections on the mirrors (in the example $N = 75$).

than 1 percent), while if it is correct the difference will be at the scale of the interferometer errors (nanometers). An even simpler method exploits the metrology on board of the piezoelectric actuator Nano-OP100. The metrology guarantees an accuracy better than 10^{-4} or to the nanometer level, so if we compare the displacement imposed to the piezo actuator with the reading of the PRA we can find the right value of N. We show in figure 15 two practical scenarios illustrating the situation. The piezo actuator was programmed to oscillate the mirror with a square wave, having arbitrarily selected amplitude of 992 nm and 496 nm p–p respectively. The p–p values measured by the PRA software were recorded (in yellow) while N was changed progressively. It is clear that only one value of N, namely $N = 75$, is correct. We note that this procedure, our preferred, has to be applied only when a realignment process of the PRA interferometer is required (e.g. after transportation). In normal use N will not change, thus can be considered a constant of the instrument.

2.3.2. Evaluating the non-linearity of the interferometer. The accuracy of the reference interferometer has been estimated theoretically and confirmed experimentally. The multiple reflections interferometer has a typical multiplication factor of about 75 (number of reflections on each mirror). That means that the periodicity of the 2π phase cycle is 633 nm/2/75 $\approx$ 4.2 nm. We have estimated that the residual non-linearity error due to non-orthogonality of the sine-cosine signals can be easily kept at 1% level by properly adjusting the retarding plates and after the normalization process. That leads to a maximum conservatively estimated error of the order of 50 pm p–p.

The real accuracy of the device could be evaluated only against an interferometer having better performances. When it is not available an alternative experimental approach can be used based on the Fourier analysis of the PRA output while a linear displacement is applied to the piezo. This classical technique consists in moving the interferometer mirror at a constant speed and observing the interferometer output in the frequency domain. Any non-linearity of the phase-displacement function will appear as a harmonic component of the output. For a given speed v (nm s^{-1}) and a non-linearity with a periodicity x (nm), the expected component in the frequency domain is at $f = v/x$ (Hz). What we expect to find in our interferometer are non-linearity with periodicity 4.2 nm, which for a speed of 100 nm s^{-1} correspond to about 24 Hz. Also, we have looked for non-linearity with a period equal to 633/2 nm which could be caused by spurious interference with light scattered by mirror surfaces. In figure 16(a) we show the output of the PRA when the actuator is driven to generate a triangular displacement, i.e. constant speed driven. In figure 16(b) the residuals from the ideal linear ramp for the two consecutive ramps highlighted in 16(a). In figures 16(c) and (d) the Fourier transforms of the interferometer output after having subtracted the linear component for two different speeds are shown. The arrows indicate the expected Fourier components for the $\approx$316 and the 4.2 nm non-linearities. No components at the expected frequencies are observed out of the background. Consistently, with what we have estimated from the distortion of the phase circle, the error is lower than 100 pm. The noise of the Nano-OP100 electronic limits this conservative result, see par. 2.2. This measurement also served as a further characterization of the Nano-OP100 regarding linearity and resolution. Indeed the residual from linearity shown in figure 16(b) are of the order of less than 3 nm p–p That is a quite good performance, considering the long stroke of the actuator.

A further confirmation that the cyclic error of the interferometer is within the estimated 50 pm p-p value is given by the experimental test described in section 3.

2.3.3. Evaluating the contribution of the noise to the uncertainty. Regarding the noise contribution, as we have discussed earlier, it depends mostly on the operation mode (open or closed loop), so in the error budget, we have to distinguish these two cases. To evaluate the contribution of the noise to the uncertainty, we have used the Allan deviation estimator.

The Allan deviation tells us the contribution of the fluctuations to the uncertainty of the measurement as a function of the measurement time. Typical Allan deviation of real measuring instruments initially decrease constantly, starting

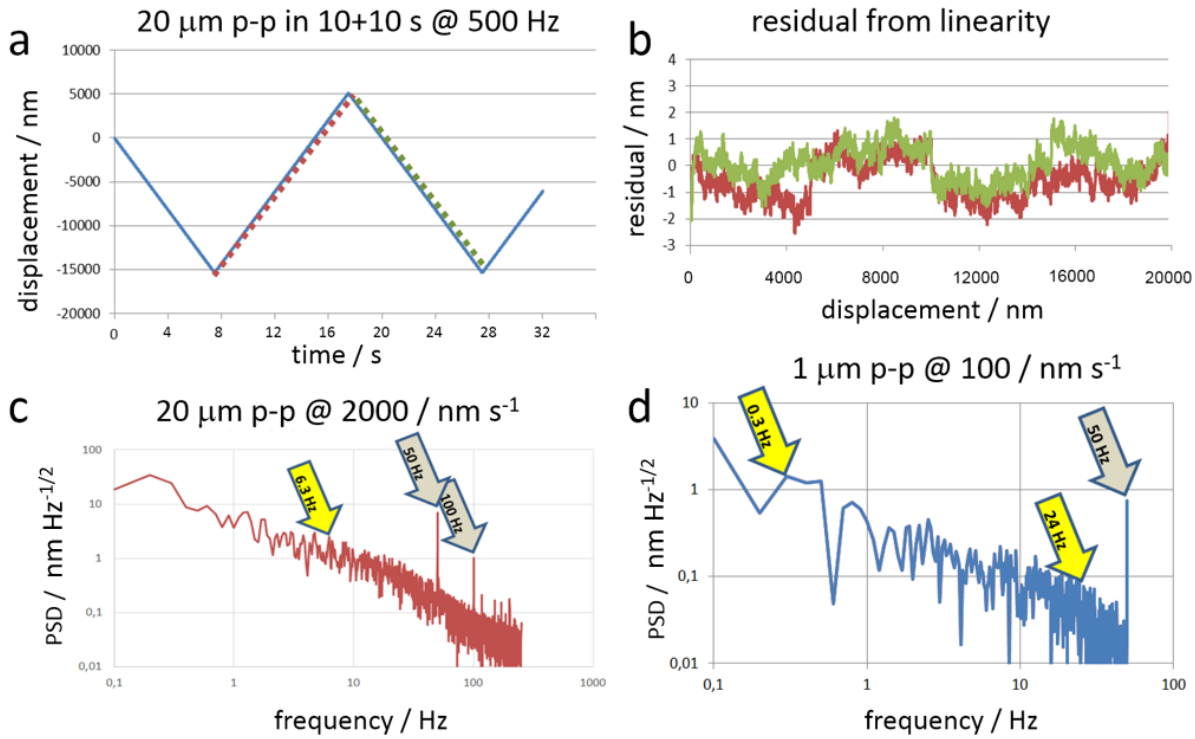

Figure 16. Linearity characterization by means of Fourier analysis. (a) Output of the PRA driven to generate constant speed ramps; (b) residual from the ideal linear ramp for the two consecutive ramps highlighted in (a); (c) and (d) Fourier transform of the interferometer output after having subtracted the linear component for two different speeds. The arrows indicate the expected Fourier components for the 316 and the 4.2 nm non-linearities. No components at the expected frequencies are observed out of the background.

from short towards long time intervals (where longer times lead to averaging more randomly distributed samples), finally tend to increase for long time intervals where the fluctuations grows with a slope larger than 1/*f* (typical thermo-mechanical drift). For these reasons, it has a minimum indicating the time interval where the measurement has less uncertainty. In figure 17 we present the Allan deviation of the temporal series of the PRA in open and closed loop mode used for the noise spectral density of the red and grey curves of figure 13. In both curves, the variance grows substantially for time intervals larger than few seconds. With the aim of defining a value for the uncertainty budget, we have considered a measurement interval shorter than 10 s and have considered the conservative values of 50 pm for the open loop mode and 0.25 nm for the closed loop mode.

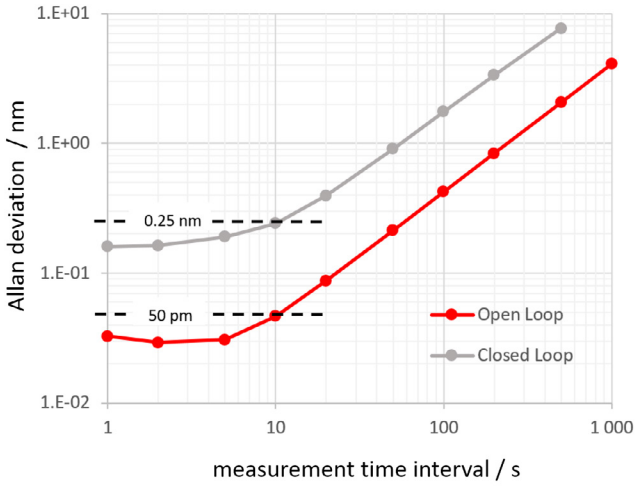

Figure 17. Allan deviation of the fluctuations of the PRA in closed and open loop modes.

2.3.4. Uncertainty budget. The uncertainty budget includes the contribution due to non-linearity (cyclic), contributions due to scale factor errors (proportional to the displacement) and terms due to noise (random and time-dependent). Because of the different nature of the contributions the error budget is dependent both on the amount of displacement and on the duration of the measurement.

If the displacement is smaller than the periodicity of the phase, i.e. at the nanometer scale or less, we can consider the phase-displacement function as a linear function, but with a slope affected by cyclic errors. We have assumed that the maximum slope deviation due to cyclic errors is 1% p–p, with sinusoidal distribution. This leads to a proportional contribution to the uncertainty of $0.01/2/\sqrt{2} \approx 3.5 \cdot 10^{-3}$. This contribution is much larger than any other scale factor, and so it is the only one which is considered in the uncertainty budget. On the other hand, the contribution of the noise in this range is dominant.

In an intermediate scale, exceeding several nanometers, we have to consider the cyclic nature of the non-linearity of the interferometer. Assuming this to be 50 pm p–p with sinusoidal distribution, we can estimate the contribution to be $50/2/\sqrt{2} \approx 18$ pm. Again we have to sum the contribution of the noise.

Table 1. Uncertainty budget. The contribution of the noise has been evaluated for a measurement time $\leqslant 10$ s. The combination of two ranges and two operating modes lead to three different budgets.

Operating mode measurement range	Open loop (sub nanometer)		Open loop (>5 nm)		Closed loop (>5 nm)	
Uncertainty contribution	Constant	Proportional	Constant	Proportional	Constant	Proportional
Non-linearity		$3.5 \cdot 10^{-3}$	18 pm		18 pm	
Noise	50 pm		50 pm		250 pm	
Wavelength				$5 \cdot 10^{-7}$		$5 \cdot 10^{-7}$
Abbe error				$2 \cdot 10^{-5}$		$2 \cdot 10^{-5}$
Misalignment				$5 \cdot 10^{-7}$		$5 \cdot 10^{-7}$
Correction factor f				$6.6 \cdot 10^{-6}$		$6.6 \cdot 10^{-6}$
Constant term	50 pm		52 pm		251 pm	
Proportional term		$3.5 \cdot 10^{-3}$		$2.1 \cdot 10^{-5}$		$2.1 \cdot 10^{-5}$
Squared combined uncertainty $\boldsymbol{u}^2$	$(50\text{ pm})^2 + (3.5 \cdot 10^{-3}\, L)^2$		$(52\text{ pm})^2 + (2.1 \cdot 10^{-5}\, L)^2$		$(251\text{ pm})^2 + (2.1 \cdot 10^{-5}\, L)^2$	

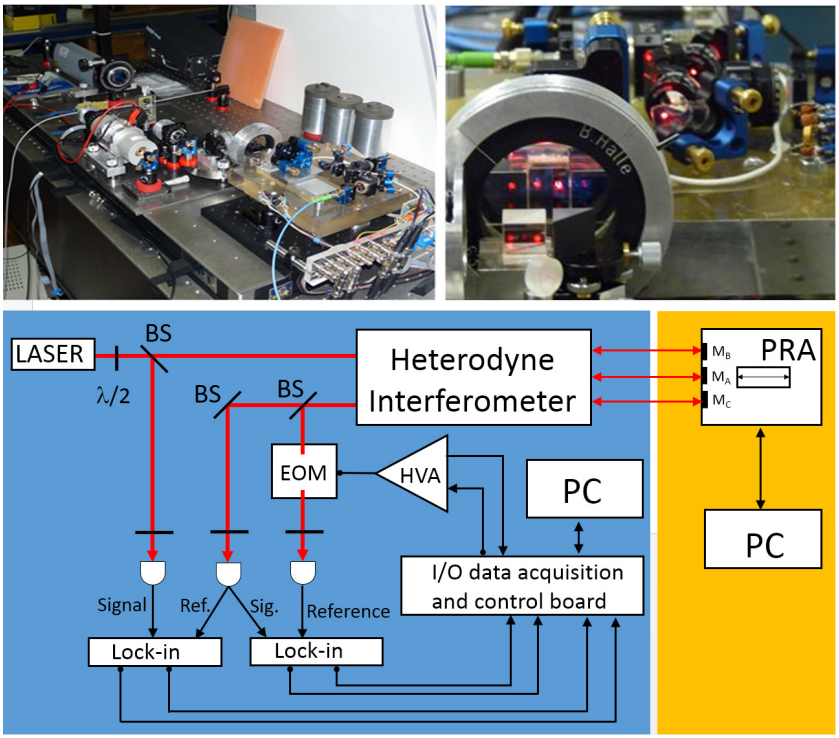

Figure 18. Set-up for the characterization of the INRIM heterodyne interferometer with the PRA. Left: scheme of the interferometer. Top right: picture of the PRA (on the front left) and the INRIM heterodyne interferometer (on the back right). Bottom right: the PRA mirrors seen from the side of the interferometer under test. Four laser spots are visible, two on the moving mirror and two on the reference mirrors.

For displacements at the micrometer scale up to the full 100 μm scale, the dominant contribution is the scale factor. The various contribution are discussed earlier. On the basis of the above considerations we present two error budgets, one for the subnanometer range the other for larger ranges.

The contribution of noise should be evaluated on the basis of the measurement time interval, but for the sake of simplicity, we decided to consider a single, yet reasonable, time interval: $T \leqslant 10$ s. So, as discussed in the previous chapter we will consider only two uncertainty values: 50 pm and 250 pm respectively for the open and the closed loop modes.

We summarize the PRA uncertainty budget in table 1. We have considered three different operative conditions: the first is in open loop mode for very small displacements, the second is in open loop mode for displacements from several nanometers to the full range, and the third is in closed loop mode.

3. Application example

One of the purposes of the PRA is to calibrate and to characterize non-linearities of other interferometers. Nanotrace project gave us the possibility to make different comparisons with other interferometers and thus to demonstrate its high accuracy.

Here we report the comparison made against a double pass heterodyne interferometer of INRIM, joining the same Nanotrace project (described in [48], page 86). The guest interferometer is placed in front of the TS. Two out of the four beams of the interferometer are reflected by the moving mirror A, while the other two are reflected by the two fixed mirrors aside B and C (see the detail in figure 18).

The following measurement test has been performed. The mirror is moved linearly while the PRA output is recorded

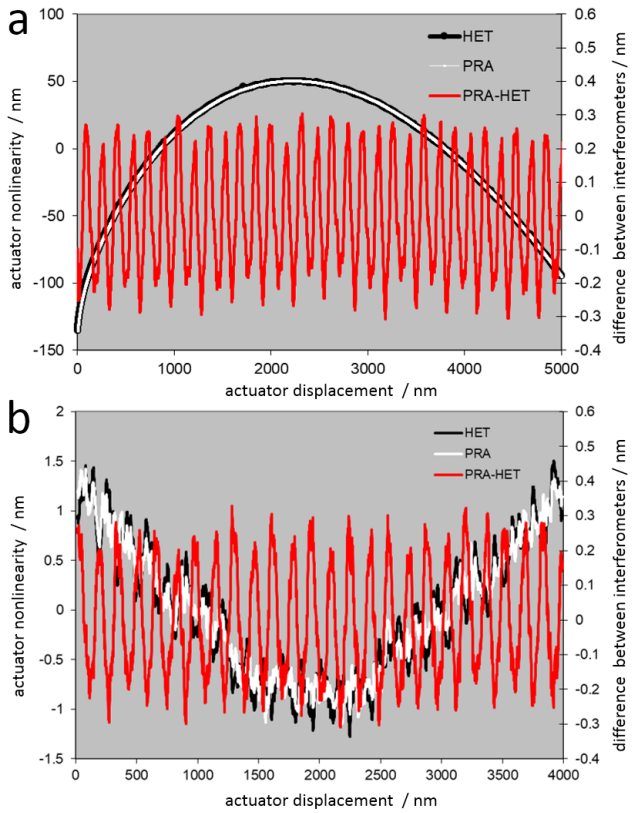

Figure 19. Characterization of a four beams heterodyne interferometer's non-linearity. Black curve and white curves are the readings of respectively the guest interferometer (HET) and the internal reference interferometer (PRA) of the movement of the piezo actuator after removing the linear part (left scale). In red the difference in the two readings (PRA-HET) highlighting the non-linearity of the interferometer under test (right scale) having $\lambda/4$ periodicity. In (a) the PRA is operating in open loop mode: the piezo non-linearity is evident. In (b) the PRA is operating in closed loop mode. The piezo non-linearity is strongly reduced, but the overall noise is increased.

together with the output of interferometer under test. The two readings, in principle identical, are then compared. In figures 19(a) and (b) the result of a typical scan are reported. In the test, the piezo actuator is displaced of about 5 μm by a linear ramp. In the case of figure 19(a) the PRA is operating in open loop mode. The PRA gain was $N = 87$. Black and white curves in the figure are the readings of the two interferometers after removing the linear component. The two curves, almost identical, show the typical non-linear behavior of the piezo actuator (about 170 nm over 5 μm). The red curve is the difference between the two readings represented in the amplified scale on the right. An evident oscillation with 158 nm periodicity is the typical cyclic non-linearity expected from a double pass interferometer (633 nm/4). A similar measurement is reported in figure 19(b) where the PRA is operating in closed loop mode. It is evident that in this case the actuator is linearized by the control loop (only 2 nm over 4 μm) which, on the other hand, has the obvious effect to increase the noise reducing the resolution of the comparison. Nevertheless, the difference between the two readings gives identical results in the two modes.

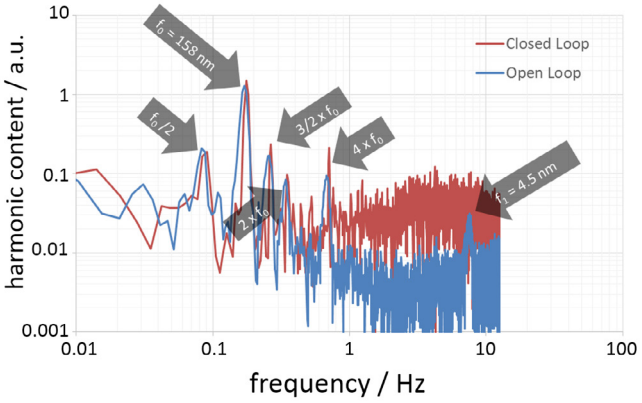

Figure 20. Fourier analysis of the difference between the output of the HET under test and the output of the PRA. The harmonic components of the HET are clearly visible. The distortion of the PRA is less than ten times smaller.

This result shows that an unknown interferometer can be accurately characterized, showing, in this case, a non-linearity of ±300 pm p–p

Similarly to the results reported in figure 16, we have performed the Fourier transform of the difference signal between the PRA and HET. We expect to find the harmonics due to distortion of the heterodyne interferometer summed to the distortion due to PRA non-linearity. In figure 20 is shown the Fourier transform of the difference signals of figure 19 (respectively in open and closed loop operation mode). The distortions of the HET are visible. Besides the expected harmonic at 158 nm, we observe a harmonic at half the frequency, due to a spurious signal at $\lambda/2$, plus various harmonics of the two. Also, a small signal, expected at the PRA harmonic, is visible in the open loop mode, while in the closed loop is covered by the noise. The result is compliant with the estimation given in 2.3.2.

4. Conclusions and outlook

A precision reference actuator (PRA) controlled by a multi-reflections interferometer and tilt sensor has been realized and characterized. The PRA composed of a low CTE ceramic glass structure where a mirror is accurately displaced with respect to a pair of fixed reference mirrors.

The device based on a long stroke piezo actuator which displacement is controlled by a multiple reflection homodyne interferometer. A custom realized three degrees of freedom pentapode actuator allows one to control the straightness of the actuator over the full range.

The PRA has 100 μm range, sub-picometer resolution, and sub-μradian straightness error. The accuracy has been conservatively estimated to be less than 50 pm p–p for small ranges (limited by the reference interferometer non-linearity) and equal to $2 \cdot 10^{-5}$ relative for long ranges, dominated by the Abbe error. The noise-limited resolution is less than 1 pm $\sqrt{\text{Hz}^{-1}}$ for frequencies larger than 3 Hz and increases to 100 pm $\sqrt{\text{Hz}^{-1}}$ for frequencies larger than 0.01 Hz.

The PRA is compact ($200 \times 200 \times 100$ mm), is easily transportable and has been mainly designed to calibrate

high-resolution interferometers. Recently the device has been used to calibrate the interferometers designed to be mounted on board of Galileo Galilei mission [49, 50] and to be used in accelerometers for space missions [51]. Thanks to its long range and very low non-linearities, its use for the calibration of any kind of high performance displacement sensors for nanometrology, such as capacitive sensors, confocal optical probes and mechanical probes, is foreseen.

Furthermore we plan to use the PRA for the accurate characterization of electrostatic actuators to be used to generate nano-forces for researches related to the new definition of the kilogram and for the measurement of the Casimir force.

In the next implementation we plan to improve the control software in order to make the PRA work in a closed loop mode where the control of the actuator is based on the output of the interferometer. This will allow us to merge the high resolution and low noise of the interferometer with the versatility of a controlled loop capable of generating any kind of controlled movement (e.g. a sinusoidal movement to calibrate an accelerometer, or a ramp to drive a microscope stage).

In conclusion, the PRA provides a toolkit for metrologists engaging with the rigor of measurement and data analysis at the nano-scale Engineering Nanometrology, from the fundamentals of precision measurement, to different measurement and characterization techniques.

Acknowledgments

The authors wish to thank their colleague Marco Santiano for his valuable technical support, their colleagues Nicola Bancone, Massimo Zucco and Milena Astrua for their support in software development and their colleague Gian Bartolo Picotto for the realization of the heterodyne interferometer used in the comparison.

The research leading to the results presented here has received funding from the European Community's Seventh Framework Programme, ERA-NET Plus, under grant agreement no 217257.

References

[1] Chiao J C *et al* 2008 Metrology and standards needs for some categories of medical devices *J. Res. Natl Inst. Stand. Technol.* **113** 121–9

[2] Di Enzo F *et al* 2016 Roadmap on biosensing and photonics with advanced nano-optical methods *J. Opt.* **18** 063003

[3] Kim Y-S, Dagalakis N G, Ferraris C and Avramov-Zamurovic S 2015 Design of a 1 DOF MEMS motion stage for a parallel plane geometry rheometer *Electronics* **19** 45–51

[4] Huang Y, Vasan A S S, Doraiswami R, Osterman M and Pecht M 2012 MEMS reliability review *IEEE Trans. Device Mater. Reliab.* **12** 482–93

[5] Novak E (ed) 2005 MEMS metrology techniques *Proc. SPIE* **5716**

[6] Jeong G-S, Bae W and Jeong D-K 2017 Review of CMOS integrated circuit technologies for high-speed photodetection *Sensors* **17** 1962

[7] Bhushan B (ed) 2010 *Springer Handbook of Nanotechnology* 3rd edn (Berlin: Springer)(https://doi.org/10.1007/978-3-642-02525-9)

[8] Hansen H N 2007 Dimensional metrology in micro manufacturing *Conference on Multi-Material micro Manufacture (4M 2007) (Borovets (Bulgaria), 3–5 October 2007)* pp 29–35

[9] Philip Garrou M K and Ramm P 2014 *Handbook of 3D Integration: 3D Process Technology* (New York: Wiley)

[10] EURAMET 2012 Science and technology roadmaps for metrology *Foresight Reference Document of the Technical Committees of EURAMET e.V—Draft Update 2012*

[11] EURAMET 2012 Dimensional metrology for micro- and nano-technologies *EURAMET Technical Report*

[12] Desai S B *et al* 2016 MoS_2 transistors with 1-nanometer gate lengths *Science* **354** 99–102

[13] Yang G, Garno J C and Liu G Y 2011 4.01—scanning probe-based lithography for production of biological and organic nanostructures on surfaces A2 *Comprehensive Nanoscience and Technology* ed D L Andrews *et al* (Amsterdam: Academic) pp 1–34

[14] Tennant D M and Bleier A R 2011 4.02—electron beam lithography of nanostructures A2 *Comprehensive Nanoscience and Technology* ed D L Andrews *et al* (Amsterdam: Academic) pp 35–62

[15] Fang Q, Sculley J, Zhou H C J and Zhu G 2011 5.01—porous metal–organic frameworks A2 *Comprehensive Nanoscience and Technology* ed D L Andrews *et al* (Amsterdam: Academic) pp 1–20

[16] Tao F and Bernasek S L 2011 5.05—self-assembled monolayers A2 *Comprehensive Nanoscience and Technology* ed D L Andrews *et al* (Amsterdam: Academic) pp 127–52

[17] Francesco M and Andrea A 2017 Metamaterial, plasmonic and nanophotonic devices *Rep. Prog. Phys.* **80** 036401

[18] Gopalakrishnan A *et al* 2012 Nanoplasmonic structures for biophotonic applications: SERS overview *Ann. Phys.* **524** 620–36

[19] Giugni A *et al* 2015 Novel plasmonic probes and smart superhydrophobic devices, new tools for forthcoming spectroscopies at the nanoscale *Nano-Structures for Optics and Photonics* ed B Di Bartolo (Dordrecht: Springer) pp 209–35

[20] Giugni A, Torre B, Allione M, Perozziello G, Candeloro P and Di Fabrizio E 2017 Hot electron nanoscopy and spectroscopy (HENs) *Conductive Atomic Force Microscopy* (New York: Wiley) pp 319–54

[21] Premaratne M and Stockman M I 2017 Theory and technology of SPASERs *Adv. Opt. Photonics* **9** 79–128

[22] Oxford instruments asylum research I. CHYPER scanning probe microscope (www.asylumresearch.com/Products/Cypher/CypherProduct.shtml#Specs)

[23] JEOL USA I *JBX-9500FS Electron Beam Lithography System* (www.jeolusa.com/PRODUCTS/Photomask-Direct-Write-Lithography/Electron-Beam-Lithography/JBX-9500FS)

[24] Scientific T F 2016 *FEI—Metrios TEM; Transmission Electron Microscope* (www.fei.com/products/tem/metrios/)

[25] Avramov-Zamurovic S, Yoo J M and Dagalakis N G 2016 Capacitive displacement sensor for detecting planar submicrometer motion *Rev. Sci. Instrum.* **87** 065001

[26] Marini M *et al* 2015 The structure of DNA by direct imaging *Sci. Adv.* **1** e1500734

[27] EMRP JRP T3.J1.4 2008 *New Traceability Routes for Nanometrology—NANOTRACE 2008* (www.emrponline.eu/selected-JRPs.html, www.nanotrace.it/Home.aspx)

[28] Marco P *et al* 2012 Comparison of the performance of the next generation of optical interferometers *Metrologia* **49** 455

[29] Bobroff N 1993 Recent advances in displacement measuring interferometry *Meas. Sci. Technol.* **4** 907
[30] Heydemann P L M 1981 Determination and correction of quadrature fringe measurement errors in interferometers *Appl. Opt.* **20** 3382–4
[31] Tanaka M, Yamagami T and Nakayama K 1989 Linear interpolation of periodic error in a heterodyne laser interferometer at subnanometer levels [dimension measurement] *IEEE Trans. Instrum. Meas.* **38** 552–4
[32] Lawall J and Kessler E 2000 Michelson interferometry with 10 pm accuracy *Rev. Sci. Instrum.* **71** 2669–76
[33] Wu C-M, Lawall J and Deslattes R D 1999 Heterodyne interferometer with subatomic periodic nonlinearity *Appl. Opt.* **38** 4089–94
[34] Joo K-N, Ellis J D, Buice E S, Spronck J W and Schmidt R H M 2010 High resolution heterodyne interferometer without detectable periodic nonlinearity *Opt. Express* **18** 1159–65
[35] TaeBong E, TaeYoung C, KeonHee L, HyunSeung C and SunKyu L 2002 A simple method for the compensation of the nonlinearity in the heterodyne interferometer *Meas. Sci. Technol.* **13** 222
[36] Jeremias S, Virpi K, Mikko M, Gian Bartolo P and Antti L 2011 A method for linearization of a laser interferometer down to the picometre level with a capacitive sensor *Meas. Sci. Technol.* **22** 094027
[37] Petr K and Petr B 2009 Common path two-wavelength homodyne counting interferometer development *Meas. Sci. Technol.* **20** 084009
[38] Vitushkin A L and Vitushkin L F 1998 Design of a multipass optical cell based on the use of shifted corner cubes and right-angle prisms *Appl. Opt.* **37** 162–5
[39] Andrew Y and Ulrich K 2012 Sub-atomic dimensional metrology: developments in the control of x-ray interferometers *Meas. Sci. Technol.* **23** 074003
[40] Basile G *et al* 2000 Combined optical and x-ray interferometry for high–precision dimensional metrology *Proc. R. Soc.* A **456** 701–29
[41] 2018 *Precision Actuators* (www.madcitylabs.com/nanopositioners.html, www.physikinstrumente.com/en/, www.nanopositioning.com/products/Nanopositioning-Actuator-Translator)
[42] Pisani M 2001 1 kV piezo amplifier keeps cost, noise low *Electron. Des.* **49** 3
[43] Pisani M 2008 Multiple reflection Michelson interferometer with picometer resolution *Opt. Express* **16** 21558–63
[44] Marco P 2009 A homodyne Michelson interferometer with sub-picometer resolution *Meas. Sci. Technol.* **20** 084008
[45] Pisani M and Astrua M 2006 Angle amplification for nanoradian measurements *Appl. Opt.* **45** 1725–9
[46] Birch K P and Downs M J 1993 An updated Edlén equation for the refractive index of air *Metrologia* **30** 155
[47] Bengt E 1966 The refractive index of air *Metrologia* **2** 71
[48] Sattler K D (ed) 2013 *Fundamentals of Picoscience* 1st edn (Boca Raton, FL: CRC Press)
[49] Nobili A M *et al* 2012 'Galileo Galilei' (GG): space test of the weak equivalence principle to 10–17 and laboratory demonstrations *Class. Quantum Grav.* **29** 184011
[50] Pisani M, Zucco M and Nobili A M 2016 Laboratory tests of a high-precision laser interferometry readout for the GG experiment in space *2016 IEEE Metrology for Aerospace (MetroAeroSpace) (22–23 June 2016)*
[51] Pisani M and Zucco M 2018 An accelerometer for spaceborne application with interferometric readout *Measurement* **122** 507–12